ACS Catalysis

pubs.acs.org/acscatalysis Research Article

Toward the Mechanistic Understanding of Enzymatic CO_2 Reduction

Ana Rita Oliveira,[‖] Cristiano Mota,[‖] Cláudia Mourato, Renato M. Domingos, Marino F. A. Santos, Diana Gesto, Bruno Guigliarelli, Teresa Santos-Silva, Maria João Romão,* and Inês A. Cardoso Pereira*

Cite This: *ACS Catal.* 2020, 10, 3844−3856 Read Online

ACCESS | Metrics & More | Article Recommendations | Supporting Information

ABSTRACT: Reducing CO_2 is a challenging chemical transformation that biology solves easily, with high efficiency and specificity. In particular, formate dehydrogenases are of great interest since they reduce CO_2 to formate, a valuable chemical fuel and hydrogen storage compound. The metal-dependent formate dehydrogenases of prokaryotes can show high activity for CO_2 reduction. Here, we report an expression system to produce recombinant W/Sec-FdhAB from *Desulfovibrio vulgaris* Hildenborough fully loaded with cofactors, its catalytic characterization and crystal structures in oxidized and reduced states. The enzyme has very high activity for CO_2 reduction and displays remarkable oxygen stability. The crystal structure of the formate-reduced enzyme shows Sec still coordinating the tungsten, supporting a mechanism of stable metal coordination during catalysis. Comparison of the oxidized and reduced structures shows significant changes close to the active site. The DvFdhAB is an excellent model for studying catalytic CO_2 reduction and probing the mechanism of this conversion.

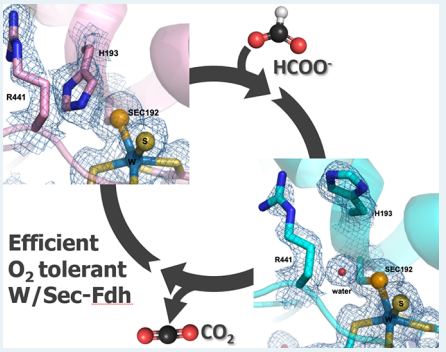

KEYWORDS: *formate dehydrogenase, CO_2 reduction, X-ray structure, oxygen-tolerance, tungsten, molybdopterin, moco*

INTRODUCTION

Developing sustainable processes to reduce the levels of atmospheric CO_2 is one of the most urgent and difficult issues facing our society. Converting CO_2 is a chemical challenge due to its intrinsic kinetic and thermodynamic stability.[1,2] Chemical conversions require high energy inputs, have low selectivity, low catalytic efficiencies, and often need rare-metal catalysts. This contrasts with the high turnovers, high specificity, and mild conditions observed in biology (through reductases, carboxylases, and lyases).[3] Studying the biochemical strategies Nature has developed to convert CO_2 is thus paramount to inspire development of more selective, efficient, and sustainable catalysts. CO_2 reduction to formate is the basis of the most energy-efficient biological pathway of carbon fixation, the reductive acetyl-CoA pathway,[4,5] which is probably also the most primordial form of carbon fixation.[6] Technologically, this reduction is of high interest as it allows CO_2 sequestration as a valuable commodity chemical (formate), providing a means of H_2 storage.[7,8] Formic acid is a safe liquid, nontoxic and nonflammable, with high volumetric energy density, and can easily be transported. Furthermore, direct formic acid fuels cells are already a reality.[8]

In biology, CO_2 reduction to formate is performed by formate dehydrogenases (FDHs). These enzymes are divided in two classes: the metal-free, oxygen-tolerant, NAD^+-dependent enzymes present in plants, fungi, and some aerobic bacteria, and the molybdenum- or tungsten-dependent enzymes present in anaerobic prokaryotes.[9−12] The metal-free, NAD^+-dependent enzymes are designed for formate oxidation (CO_2 reduction from NADH is thermodynamically uphill), and are extremely slow in the reductive direction. In contrast, both the Mo- and W-dependent FDHs catalyze CO_2 reduction,[13−16] even in the case of the NAD(H)-dependent, multimeric Mo-FDHs.[17,18]

In the metal-dependent FDHs, the active site consists of a Mo/W atom coordinated by two Molybdopterin Guanine Dinucleotides (MGD), one selenocysteine (Sec) or cysteine residue and one terminal sulfido (=S/—SH) ligand. The sulfido ligand is introduced by a dedicated chaperone and is essential for activity.[19−21] Despite considerable studies, the mechanism used by FDHs to oxidize formate or reduce CO_2 is still unclear. Several proposals have been made, and the topic has raised considerable debate.[11,12,22−24] Critical issues still under discussion are (i) whether the Sec/Cys ligand dissociates from the metal during catalysis and is replaced by formate,[22,23,25−28] or if metal coordination is maintained during catalysis;[15,29,30] and (ii) whether oxidation of formate involves hydride transfer to the metal or sulfido group,[15,26,29,30] or C_α proton abstraction by a protein residue.[28,31] A number of experimental and computational tools have been explored to try to elucidate this mechanism, namely X-ray crystallography,[23,31−33] X-ray absorption spectroscopy,[21,34,35] EPR,[29,36−38] theoretical calculations,[26,27,30] and inhibition studies.[22,28,39] However, the results

Received: January 6, 2020
Revised: February 15, 2020
Published: February 27, 2020

https://dx.doi.org/10.1021/acscatal.0c00086
ACS Catal. 2020, 10, 3844−3856

are not always conclusive due to the difficulty in confidently assigning the observations to relevant catalytic states, compounded by the intrinsic instability of the proteins, which may be present in inactivated states. There is, thus, an urgent need for detailed structural information on FDHs in different catalytic/redox states.

When focusing on CO_2 reduction to formate it seems logical to investigate FDHs that physiologically perform this function, rather than formate oxidation. This is the case of enzymes present in acetogens, which grow from converting CO_2 to acetate,[4] in syntrophs, which produce formate and H_2 as vehicles for interspecies electron transfer,[40] and finally in the closely related sulfate reducing bacteria, which in the absence of sulfate also turn to a syntrophic lifestyle.[41] In fact, the enzymes with the highest CO_2-reducing activities are all derived from these organisms, and include the hydrogen-dependent CO_2 reductases (HDCR) from the acetogens *Acetobacterium woodii* and *Thermoanaerobacter kivui*,[14,16] the W-FDH from the syntroph *Syntrophobacter fumaroxidans*,[13,42] and the Mo-FDH from the sulfate reducer *Desulfovibrio desulfuricans*.[15]

Here, we report a novel expression system for production of a W/Sec-FDH from the sulfate reducer *Desulfovibrio vulgaris* Hildenborough, DvFdhAB, and its catalytic and structural characterization. The DvFdhAB is responsible for CO_2 reduction in *D. vulgaris*[43] and is the main FDH expressed in this organism if tungsten is available,[44] revealing its physiological preference over the Mo-containing isoenzymes. In contrast to other high-activity FDHs containing W and/or Sec that need to be purified anaerobically,[14,16,42] the DvFdhAB exhibits a remarkable oxygen tolerance, as it can be purified and handled aerobically. Its high activity, robustness, and simple composition make it an ideal model for biocatalytic applications. We report here the catalytic characterization of the DvFdhAB, inhibition studies and the crystal structures in the oxidized and reduced states. These results bring important information toward elucidating the catalytic mechanism of metal-dependent FDHs.

RESULTS

Expression System. Two different strategies were tested for production of recombinant DvFdhAB: tag-labeling of the *fdhA* gene (DVU0587), and complementation of a Δ*fdhAB* deletion mutant with an expression vector. For the first strategy, a suicide vector was constructed based on pMO719,[45] to directly modify *fdhA* in the genome (Figure S1A of the Supporting Information, SI). In the second approach, we used the *D. vulgaris* Hildenborough Δ*fdhAB* deletion strain,[43] for which a complementation vector, pRec-FdhAB-Strep was assembled (Figure S1B). The expression of FdhA was confirmed in both systems (Figure S2). The formate oxidation activity of the complemented strain was approximately three times higher than that of the genome-modified strain. Thus, DvFdhAB was routinely produced using the complementation strategy.

Purification and Activation Behavior. Both W and Sec-containing enzymes are catalytically more active than their Mo and Cys counterparts, but they usually suffer from being extremely oxygen-sensitive.[42] Remarkably, the W/Sec-DvFdhAB could be purified and handled under aerobic conditions. Nitrate and glycerol were used as stabilizing agents. Nitrate is an inhibitor that helps to protect the enzyme,[17] presumably by preventing loss of the labile sulfido group.[29,46] As desired, a single affinity chromatography step was enough to produce pure DvFdhAB (Figure S3). Identical reduction levels were obtained with formate as with dithionite (Figure S4), indicating that the enzyme is fully loaded with the tungsten-sulfido group (W=S/−SH), essential for reduction by formate.

Metal-dependent FDHs often require reductive activation to display maximal activity.[15,47] In contrast to the *D. desulfuricans* Mo/Sec-FdhABC,[15] a 30 min incubation with formate was not enough to fully activate DvFdhAB, as a significant lag phase was still observed (Figure S5). Preactivation for 30 min with both formate and DTT abolished this lag phase. Furthermore, just 5 min preincubation of DvFdhAB with 50 mM DTT (or TCEP) was enough to observe maximum initial activities, indicating full activation.

Enzyme Kinetics. DvFdhAB oxidizes formate with a turnover rate of 1310 ± 50 s^{-1} (Table 1). In contrast to a previous report[44] where DTT preactivation was not used, the DvFdhAB is in fact highly active in catalyzing CO_2 reduction with a turnover of 315 ± 28 s^{-1}. This robust CO_2-reducing activity agrees with the fact that in vivo this enzyme is responsible for formate production, when W is available.[43] The activity of native DvFdhAB^{WT} was revaluated in the new assay conditions, showing similar rates to the recombinant version: a turnover of 1104 ± 62 s^{-1} for formate oxidation, and of 304 ± 41 s^{-1} for CO_2 reduction. These high catalytic activities place the W/Sec-DvFdhAB among the most active CO_2 reductases yet reported.

Table 1. Kinetic Constants of *D. vulgaris* DvFdhAB

DvFdhAB	$HCOO^-$ oxidation	CO_2 reduction
specific activity	568 ± 22 Umg^{-1}	137 ± 12 Umg^{-1}
turnover	1310 ± 50 s^{-1}	315 ± 28 s^{-1}
K_M	16.9 ± 2.8 μM	420 ± 47 μM (CO_2)

The DvFdhAB pH optimum for formate oxidation is 7.6, but activity is sustained close to 80% between pH 7 and 10 (Figure 1). The pH optimum of the reductive reaction is 7.1, and the activity is held above 60% between pH 4.7 and 7.6. Due to the influence of carbonate on the pH (see SI text), the CO_2 concentration varies across the pH range. With 50 mM sodium bicarbonate as the CO_2 source the concentration of CO_2 (l) is only 3.6 mM at pH 7.5, and decreases drastically above that, to only 120 μM at pH 9. In addition, the ionic strength of the solution also increases at higher pHs, which may also have a detrimental effect on activity.[18] These two factors likely explain the drastic drop in activity above pH 7. The kinetic constants were determined for both reactions at the pH optimum (Figure 1C/D, Table 1). The K_M for formate is 16.9 ± 2.8 μM at pH 7.6, which is in the same order of magnitude as *S. fumaroxidans* W-Fdhs,[42] and significantly lower than the K_M of the *A. woodii* Mo-FdhF2 or *E. coli* Mo-FdhH, which are in the mM range.[14,48] The K_M for CO_2 is 420 ± 47 μM (see SI text). The only FDH reported with higher CO_2 affinity is the *D. desulfuricans* Mo-FDH, with a K_M of 15.7 μM.[15] However, this value was calculated by a linearized graphical method, which can introduce significant errors.

Inhibition by nitrate was tested, since this was used as stabilizing agent. DvFdhAB retains 40% of formate oxidation and 60% of CO_2 reduction activity in the presence of 100 mM nitrate, so this is a very weak inhibitor. Since the enzyme is diluted in the activity assays (at least 100×), the effect of nitrate in these assays will be negligible. Azide is a stronger inhibitor and at 10 mM it reduced the oxidative rate to only 7%, whereas about 45% activity was sustained for CO_2 reduction. Thus, as reported for *E. coli* FdhH,[22] the DvFdhAB is more strongly inhibited in

https://dx.doi.org/10.1021/acscatal.0c00086
ACS Catal. 2020, 10, 3844−3856

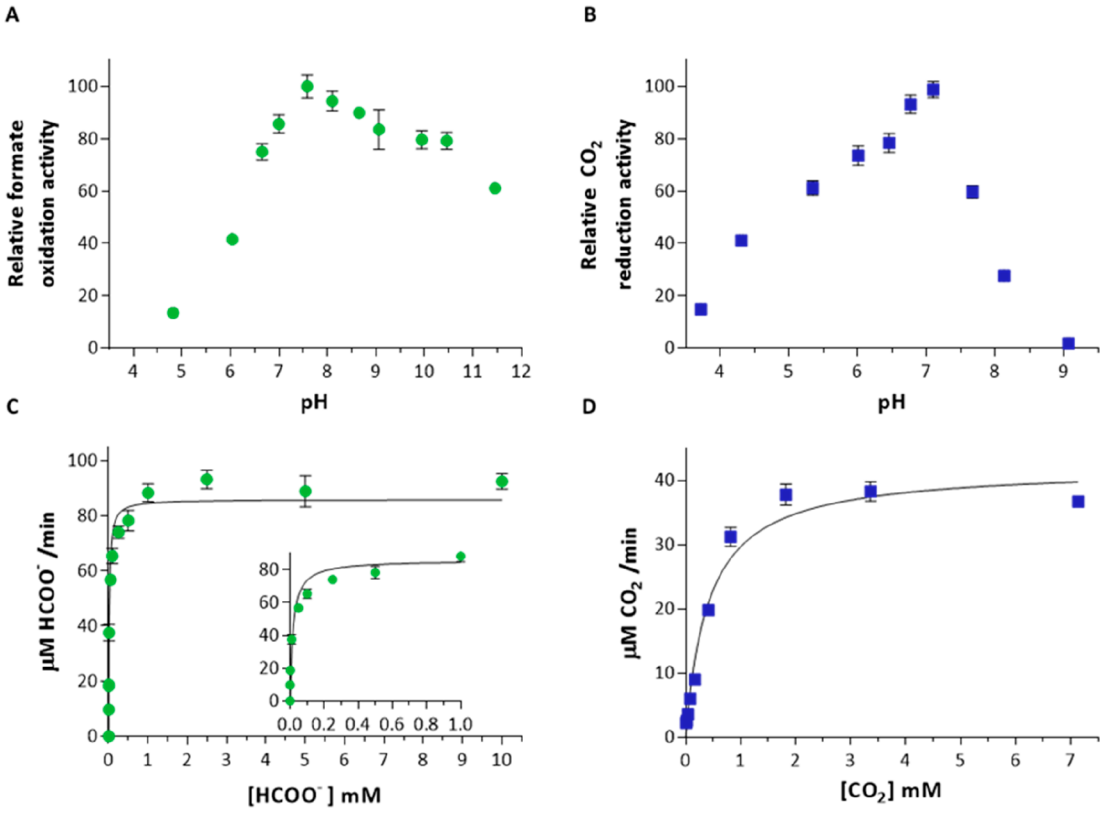

Figure 1. Kinetic characterization of DvFdhAB. (A) Effect of pH on formate oxidation activity (20 mM formate) and (B) on CO_2 reduction activity (with 50 mM sodium bicarbonate). (C) Steady-state formate oxidation kinetics and (D) steady-state CO_2 reduction kinetics. Lines represent the direct fitting of Michaelis−Menten equation to experimental data. All assays were performed in triplicate, and the error bars show the standard deviation.

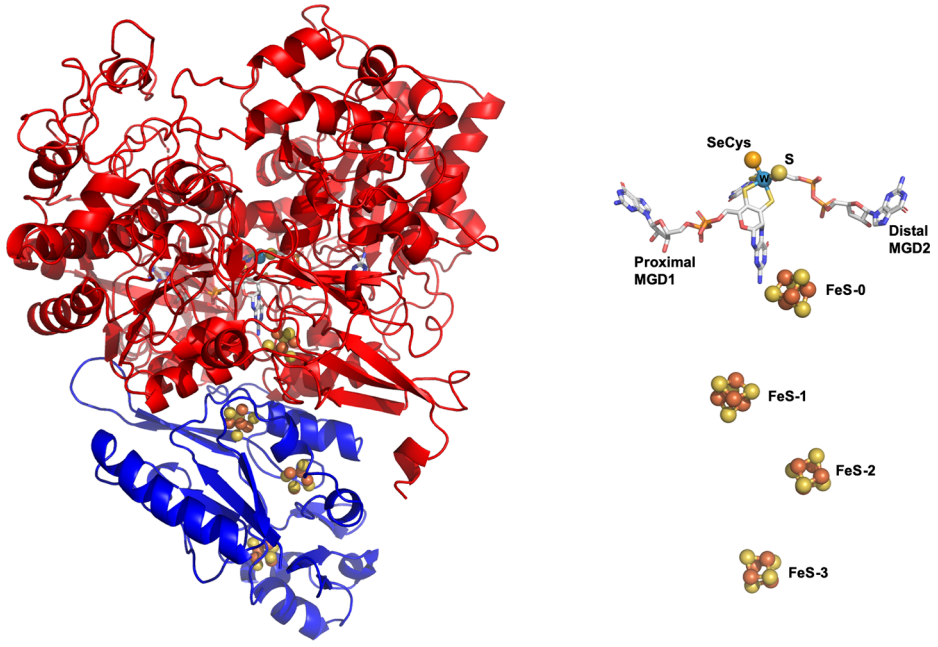

Figure 2. DvFdhAB structure. (Left) Structure of the heterodimer (α-subunit, red and β-subunit, blue). (Right) The metal cofactors, $W(MGD)_2$ and four [4Fe-4S] centers.

the oxidized W(VI)═S than in the reduced W(IV)−SH state. We could not detect any activity for nitrate reduction, in contrast to the *R. capsulatus* enzyme.[28]

Stability and Oxygen Tolerance. The stability of FDHs is critical for their use in biotechnological applications. DvFdhAB is quite thermostable, with a melting temperature of 77.3 ± 1.0 °C, which is increased to 79.8 ± 0.2 °C in the presence of nitrate and glycerol. Storage of the as-isolated pure DvFdhAB at 4 °C or −20 °C in aerobic conditions did not lead to loss of activity even after 30 days (Figures S6 and S7). When kept aerobically at

https://dx.doi.org/10.1021/acscatal.0c00086
ACS Catal. 2020, 10, 3844−3856

room temperature, the activity was stable for at least 10 h (Figure S8). However, when the enzyme was reduced by formate the activity was lost within 4 h of air exposure, and in the absence of nitrate and glycerol the loss occurred in less than 2 h. In contrast, under anaerobic conditions the formate-reduced enzyme maintains its activity even after 48 h (Figure S9). Overall, the oxidized enzyme is highly stable, which has already been exploited in semisynthetic systems for light-driven CO_2 reduction.[49,50]

Crystal Structures in Oxidized and Formate-Reduced States. For a mechanistic understanding of FDHs it is essential to have detailed structural information. There are only a few reported structures, from *E. coli* FdhH[23,31] (EcFdhH), *E. coli* FdhN[32] (EcFdhN), and *Desulfovibrio gigas* FdhAB (DgFdhAB),[33] and only one of these is from a reduced state (EcFdhH).[31] This structure was later reinterpreted[23] revealing, unexpectedly, the dissociation of Sec from metal coordination, and the possible presence of mixed states at the active site. It is thus essential to get additional crystal structures of FDHs, particularly in the reduced state. The DvFdhAB was crystallized aerobically (oxidized form), as well as in an anaerobic chamber in the presence of formate (reduced form). The crystals of the oxidized form (DvFdhAB_ox, 6SDR) diffracted beyond 2.1 Å (Table S2), and the structure was solved by molecular replacement, using the *D. gigas* FdhAB structure[33] as the search model. The model was traced and refined to final crystallographic R_{work} and R_{free} values of 18.6% and 22.6%, respectively, with good geometry. Crystals of the formate-reduced form (DvFdhAB_red, 6SDV) diffracted beyond 1.9 Å, and the structure was solved by molecular replacement using the oxidized form as search model. The model was refined to final crystallographic R_{work} and R_{free} values of 15.9% and 19.7%, respectively, with good geometry (Table S2).

The DvFdhAB is a heterodimer (Figure 2) and can be divided into four (FdhA) plus three (FdhB) domains (Figure S10), following the classification of DgFdhAB. The large, catalytic α subunit harbors the [W(MGD)2, SH, Sec] cofactor and one [4Fe-4S] cluster, while the small β subunit contains three [4Fe-4S] clusters. The overall structure of the catalytic subunit is very similar to those of DgFdhAB and EcFdhN, with RMSDs of 1.30 Å for 957 α-carbons and 2.01 Å for 947 α-carbons, respectively.

As in other enzymes from the DMSO reductase family, the $W(MGD)_2$ cofactor is deeply buried inside the protein and stabilized by an extensive network of hydrogen bonding and hydrophobic interactions. The proximal MGD1 interacts with domains II and IV and is the only one involved in electron transfer. The closest pathway is via the exocyclic NH_2 of the pterin and the FeS-0 center, mediated by the N^{ζ} of highly conserved Lys90. The distal MGD2 interacts with domains II and IV and is very likely involved in modulating the redox potential of the metal (see below).

The electron transfer β-subunit holds three [4Fe-4S] clusters and interacts with the large subunit covering a surface of ca. 2066 $Å^2$ (PDBePISA protein−protein interaction server; http://www.ebi.ac.uk/msd-srv/prot_int/). Several hydrophobic interactions, salt bridges, hydrogen bonds, and tightly bound water molecules stabilize the interface between the two subunits. This interaction involves over 60 residues of domains I, II, III ,and IV in the large subunit and 50 amino acids in the small subunit. The overall structure of the β-subunit is very similar to those of DgFdhAB and EcFdhN, with rmsds of 1.08 Å for 215 α-carbons and 2.35 Å for 208 α-carbons, respectively. The major difference is observed in loop 58−66 in DvFdhAB that is one residue longer than that in DgFdhAB, and is involved in an additional hydrophobic interaction with the α-subunit.

Active Site in Oxidized and Reduced Forms. The DvFdhAB catalytic pocket and respective entrance tunnel is positively charged, and three glycerol molecules are modeled in this cleft (Figure 3). The glycerol closest to the W is hydrogen bonded by Ser194 and His457, the second glycerol is oriented by Arg441, Thr450, and a water molecule oriented by Tyr462. The third glycerol is found in the tunnel entrance, oriented by Gly207 backbone nitrogen and water molecules that make bridges with Trp492 and Arg206. These glycerol molecules probably mimic transit formate binding sites and shed light on the formate entrance/release mechanism.

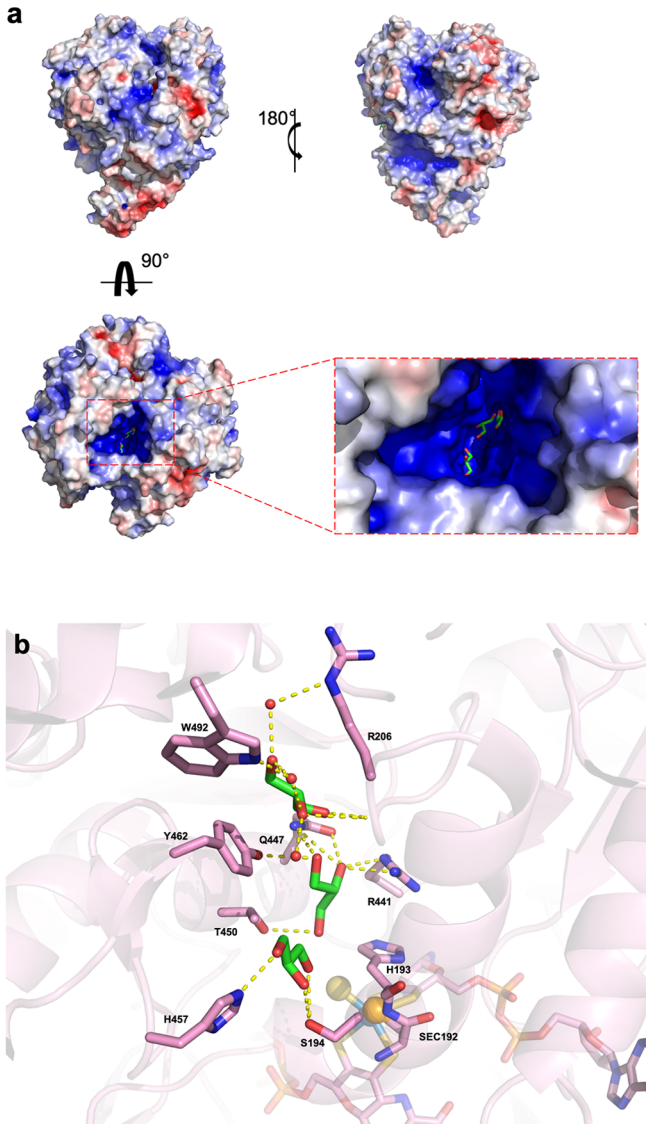

Figure 3. Protein surface charges and active site cavity. (a) Electrostatic potential mapping on DvFdhAB surface and active site pocket (oxidized form). The electrostatic potential was calculated using PyMOL's APBS plugin. Electropositive regions are colored blue, electronegative regions are colored red, and regions of neutral charge are colored white. Three glycerol molecules (green) were modeled in the tunnel leading to the catalytic pocket. (b) Detail of the substrate tunnel and active site, showing the interactions of the three glycerol molecules.

https://dx.doi.org/10.1021/acscatal.0c00086
ACS Catal. 2020, 10, 3844−3856

The W center is fully loaded with metal (Figure S11) according to the relative B factors for a full occupancy of all atoms (Table S2), and is buried 30 Å away from the protein surface. In the oxidized form (DvFdhAB_ox), the metal is hexacoordinated to four sulfur atoms from the two dithiolenes, a selenium from Sec192 and a sulfur ligand (W−SH/═S), in a distorted octahedral geometry (Figure 4a and S11). In the vicinity of the metal there are two highly conserved amino acids, His193, establishing a π interaction with the Se from Sec192, and Arg441, which establishes a hydrogen bond with one of the glycerol molecules, and has been proposed to be responsible for orienting the substrate molecule.[23]

In the formate-reduced form (DvFdhAB_red), the environment surrounding the active site suffers a conformational rearrangement (Figure 4b,c). The Sec192 loop (Ile191-His193) suffers a distortion, and the Sec192 Cα atom shifts up to 1.00 Å from the position occupied in the oxidized form. Part of an adjacent α-helix (Ser194-Pro198) is also displaced up to 2.25 Å ($Thr196^{ox}$−$Thr196^{red}$, Cα−Cα distance; not shown on figure for clarity). However, Sec192 remains coordinated to the metal (Figure S11b). Remarkably, the catalytically relevant His193 moves away from the active site adopting a different rotamer, and a water molecule occupies the previous position of the imidazole ring, 3.18 Å away from Se, establishing a hydrogen bond with Gly442 amide bond. In addition, Arg441 side chain also suffers a small rearrangement. The Sec192 loop shift is propagated to neighboring amino acids from different domains with the consequent displacement of the adjacent hydrophobic Ile191 that promotes the tilt of the side chains of Trp533, Phe537, and Phe160.

To further confirm the W redox state in the formate-reduced crystals, we performed EPR spectroscopy on a sample prepared with small crystals spread in cryoprotectant solution, in parallel with a dissolved sample. Due to the random orientation of crystals in the polycrystal sample, the EPR spectrum can be directly compared to that given by a frozen solution.[51] At 15 K the EPR spectra showed the $[4Fe{-}4S]^{+/2+}$ clusters of both samples in a fully reduced state (Figure S12). These signals broaden above 50 K and are no longer detected at 80 K. At this temperature no slow relaxing W(V) signal is detected in either sample, confirming that formate leads to full reduction of the protein to the W(IV) state, which is EPR silent. Very weak features are observed between g = 1.92 and 1.89 at T = 80 K but they cannot be assigned to a minor proportion of W(V) species.

Finally, conformational changes are also observed for the two MGDs cofactors and surrounding environment, which are more pronounced for the distal MGD2. In the oxidized form, Gln890 is in close contact to MGD1, via a hydrogen bond to N5 of the piperazine central ring (assuming a tetrahydro form, Figure 4a). Additionally, Gln890 NH_2 is a H-bond donor to one of the dithiolene sulfur atoms and to the carboxylate of Glu443 (Figure S13). In the reduced form, Gln890 adopts a new rotamer and establishes a hydrogen bond to Glu443, which also adopts a different conformation (Figure S13). The interaction with the dithiolene sulfur atom is maintained. In contrast, the Gln890 C═O group is now stabilized by an interaction to a water molecule present only in the reduced structure (Figures 4b and S13). This water molecule is hydrogen bonded to O1A, O5′, and O4′ from the dinucleotide part of MGD2. All these movements seem to promote a major distortion of the ribose moiety. Gln890 and Glu443 are conserved in sulfate reducers, and in the DgFdhAB_ox structure their positions are conserved. A similar situation is observed in arsenite oxidase where a corresponding

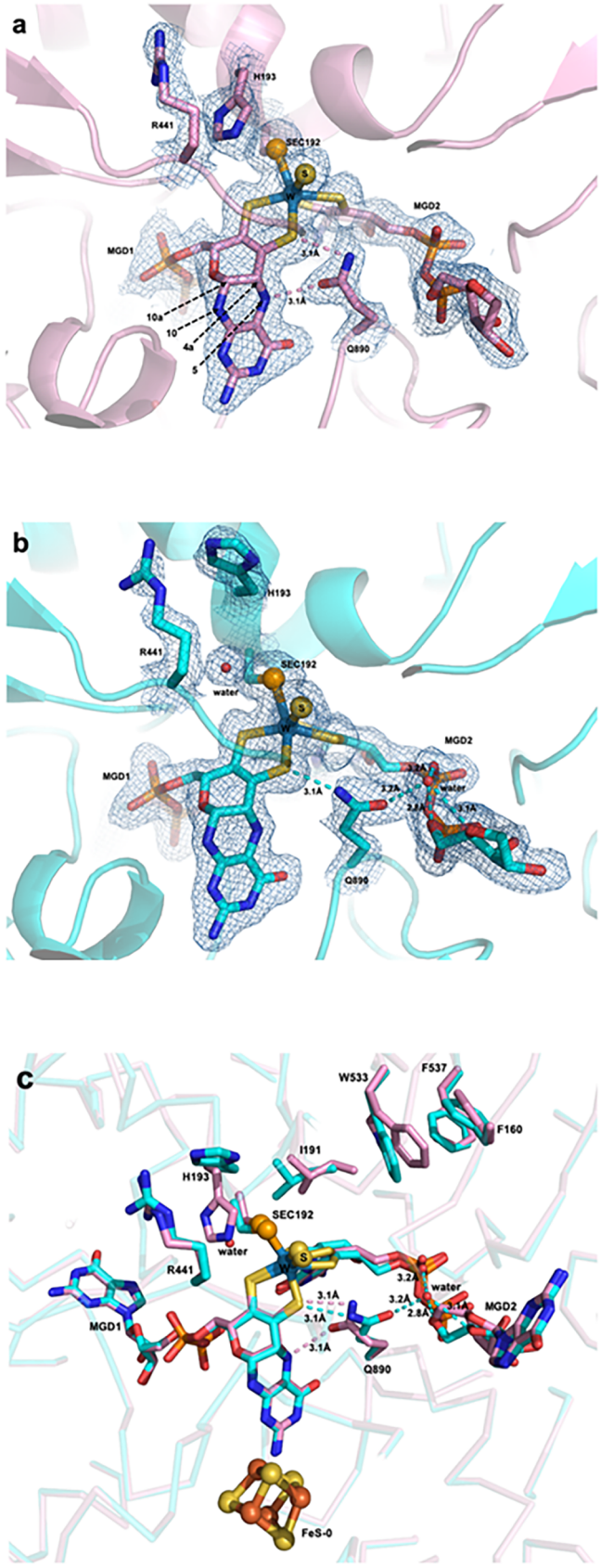

Figure 4. DvFdhAB active site. (a) Close-up view of the DvFdhAB_ox active site and 2Fo-Fc electron density map contoured at 1σ; (b) close-up view of the DvFdhAB_red active site and 2Fo-Fc electron density map contoured at 1σ. (c) Superposition of the active sites of oxidized (pink) and reduced (cyan) forms.

https://dx.doi.org/10.1021/acscatal.0c00086
ACS Catal. 2020, 10, 3844−3856

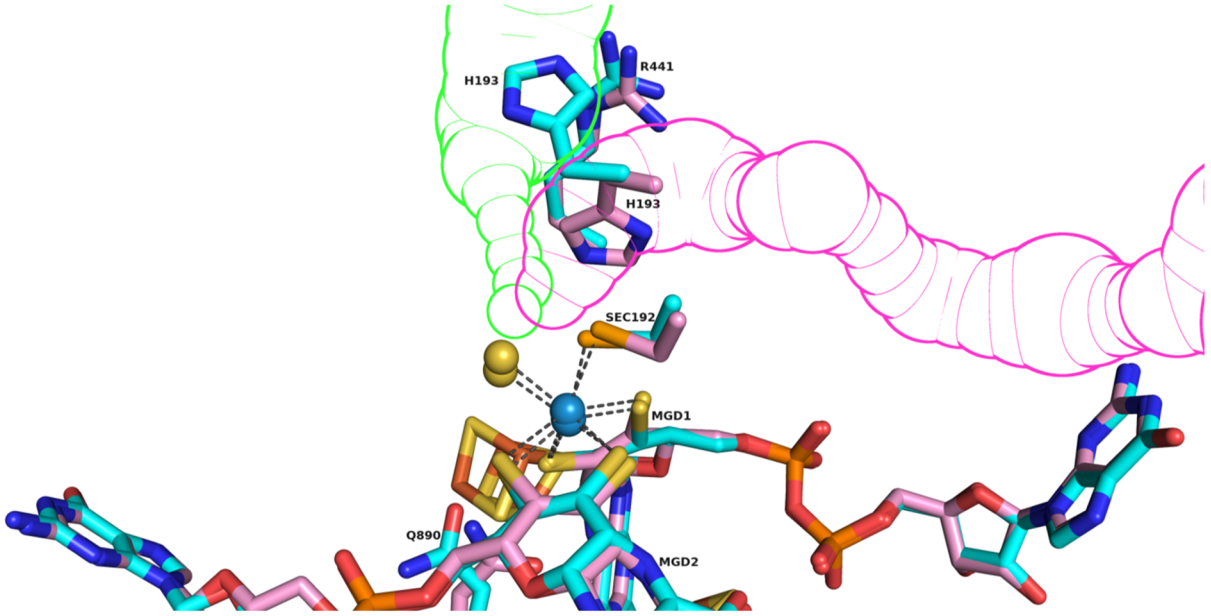

Figure 5. Proposed formate and CO_2 tunnels. The formate tunnel is represented in green and the CO_2 tunnel is represented in magenta. The imidazole ring of His193 is shown in pink (oxidized form) and in cyan (reduced form).

Gln is also interacting with N5 of the MGD1 pterin.[52] In other reported FDH structures the residue corresponding to Gln890 is replaced by a Ser (EcFdhH) or by a His (EcFdhN and EcNarG[53]). Rothery and co-workers assigned a "bridging" role to this residue (Gln, Ser or His) providing H-bond interconnection between both pyranopterins.[54] In these structures (EcFdhH ox and red) the "bridging" residue Ser587 also changes its rotamer but the smaller side chain precludes a close interaction to the MGD1 pterin.

Formate and CO_2 Tunnels. The tunnel network within the catalytic subunit was inspected with CAVER for both oxidized and reduced structures. In the oxidized form, the calculated tunnel with highest score links the positively charged funnel to the active site, assigned as the formate tunnel (Figure S14a), with a minimal diameter of 1.4 Å and a length of 13.2 Å. Strikingly, the tunnel with the highest score for the reduced structure, assigned as the CO_2 tunnel, is different (Figure S14b). It displays a minimal diameter of 1.8 Å and length of 39.7 Å, and also links the W active site to the protein surface. The surface of this tunnel is mainly composed by hydrophobic amino acids, and therefore it is likely to allow the access/release of nonpolar molecules such as CO_2. As discussed above, the imidazole ring of the conserved active site His193 is in a different position in oxidized and reduced structures. In the oxidized form its position closes the hydrophobic CO_2 tunnel, while in the reduced form His193 flips toward the formate tunnel opening the hydrophobic one and blocking the entrance of new formate molecules (Figure 5). Thus, the formate and CO_2 tunnels seem to be mutually exclusive, with His193 acting as a switch between the two.

The predicted tunnels are supported by analysis of amino acid conservation among the group of periplasmic NAD^+-independent FDHs (which are phylogenetically separate from the cytoplasmic ones)[55] (Figure S15). The positively charged tunnel, for formate access/release, is composed by amino acids that present a high degree of conservation (at least 70% identity), whereas the hydrophobic tunnel presents a lower degree of conservation.

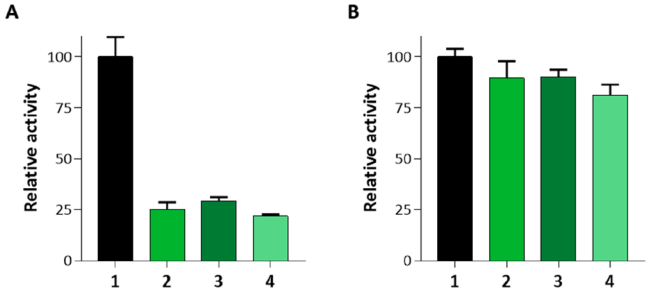

Figure 6. Inhibition by iodoacetamide. Formate oxidation activities after 30 min incubation without IAA (1), with 20 mM IAA (2), with 20 mM IAA and 20 mM formate (3), and with 20 mM IAA and 20 mM Nitrate (4) at pH 7.6 (A) and pH 9 (B). The activities were normalized to (1).

Inhibition by Iodoacetamide. Previous reports of Sec/Cys alkylation by IAA in *E. coli* FdhH[39] and the *R. capsulatus* Mo-Fdh[28] were taken as indication that the Sec/Cys residue dissociates during catalysis. Since the DvFdhAB_red structure indicates that Sec remains bound to W in this state, we tested the effect of iodoacetamide (IAA) alkylation on the activity. Incubation of DvFdhAB with IAA at pH 7.6 resulted in 75% inhibition of the formate oxidation activity (Figure 6). Contrary to *E. coli* FdhH[39] and *R. capsulatus* Mo-FDH,[28] this inhibition was not dependent on the presence of substrate. At pH 9, the IAA inhibition is considerably lower, but also no effect of substrate or inhibitor was observed. The IAA-treated samples were analyzed by mass spectrometry to reveal which residues were alkylated (Table S3). In all samples nine Cys are always alkylated (seven Cys coordinating FeS clusters, and two near the protein surface), which explains the inhibition observed. A peptide containing the IAA-alkylated Sec192 was not detected in any of the samples. Instead, all of the samples contained a peptide where Sec is modified to dehydroalanine. This modification is frequently identified in Sec-containing peptides, resulting from the loss of selenium during the MS sample preparation and analysis.[56,57] If IAA-alkylation of Sec had

https://dx.doi.org/10.1021/acscatal.0c00086
ACS Catal. 2020, 10, 3844−3856

happened, then this would prevent loss of selenium and the alkylated peptide would be easily identified.[56] This result suggests that the selenol ligand of DvFdhAB is not accessible for reaction with IAA, confirming the structural observations.

DISCUSSION

CO_2 reduction by FDHs can vary by orders of magnitude, and in the metal-dependent enzymes is often extremely oxygen sensitive. The metal at the active site is one important determinant for the level of this activity. Although the chemistry performed by Mo is similar to that of W, W(IV) is a stronger reductant than Mo(IV), and this is likely one of the reasons for the higher reductive catalytic efficiency of W-FDHs. Another important determinant is the presence of Sec versus Cys as metal-coordinating residue. In *E. coli* FdhH a Sec/Cys variant showed more than 2 orders of magnitude lower turnover than the native enzyme, and was suggested to be directly involved in the reaction.[39] A similar effect has been observed for a Sec/Cys variant of the *D. vulgaris* Hildenborough [NiFeSe] hydrogenase, where the Sec was additionally shown to be essential for the oxygen tolerance of the enzyme.[58]

The homologous expression system reported here allows production of high levels of the W/Sec-DvFdhAB fully loaded with cofactors. The simple composition of this enzyme, coupled with its high activity and high stability, enabling aerobic handling, make this enzyme an ideal model system for catalytic and mechanistic studies of CO_2 reduction. In fact, the enzyme has recently been explored for photocatalytic CO_2 reduction coupled to Photosystem II,[49] or dye-sensitized TiO_2[50] in the first report of visible light-driven CO_2 reduction without redox mediators.

The W/Sec-DvFdhAB is among the most active enzymes for CO_2 reduction. These include the trimeric W/Sec-Fdh1 from the syntroph and sulfate reducer *S. fumaroxidans*. Its turnover for CO_2 reduction was initially reported as 2460 s^{-1},[42] but was later revaluated to 282 s^{-1}.[13] This enzyme is highly oxygen-sensitive, requiring anaerobic isolation. Another example is the Hydrogen-Dependent Carbon dioxide Reductase (HDCR) from *A. woodii* that uses molecular hydrogen for the reduction of CO_2.[14] This multisubunit complex comprises one [FeFe]-hydrogenase, two electron transfer subunits and a Mo/Sec-FDH (FdhF2). The hydrogenation of CO_2 is catalyzed by HDCR at a rate of 28 s^{-1}, but the CO_2 reduction activity of FdhF2 from MV^+ is 372 s^{-1}, similar to DvFdhAB. An HDCR from the thermophile *T. kivui*, containing a W/Cys-FDH displays even higher activity for CO_2 hydrogenation at 60 °C (2657 s^{-1}),[16] but curiously a lower formate oxidation activity (1337 s^{-1}) than the *A. woodii* enzyme (1690 s^{-1}). Again, this enzyme has to be isolated and handled anaerobically, and despite its thermotolerance shows some stability issues. The trimeric *D. desulfuricans* Mo/Sec-FdhABC can be isolated and handled aerobically, but its CO_2 reduction activity (47 s^{-1})[15] is 1 order of magnitude lower than that of DvFdhAB. Still, the activity of these enzymes is much higher than those of the oxygen-tolerant NADH-dependent enzymes, with the highest activities reported for the *Rhodobacter capsulatus* (1.5 s^{-1})[17] and *Cupriavidus necator* enzymes (11 s^{-1}).[18] In this context, the W/Sec-DvFdhAB stands out as a unique model system, combining high catalytic activity with good stability, enabling aerobic handling.

The stability profile of DvFdhAB allowed the enzyme to be crystallized in two different redox states. This has previously been achieved only for *E. coli* FdhH,[31] a cytoplasmic enzyme that is part of the formate-hydrogen lyase (FHL) complex and which belongs to a different phylogenetic group.[55] The structure of the DvFdhA catalytic subunit is quite similar to that of the four available FDH crystal structures (rmsd 1.90 Å all atoms), with the largest differences found between DvFdhAB and *E. coli* FdhH, which has an additional long C- terminus helix. The active sites are also very conserved, independently of having W or Mo. In all available crystal structures, the protein W/Mo ligand is a Sec and the sixth ligand is a sulfur (although not corrected in the PDB for earlier deposited structures, 1FDO and 1kQF, where an oxygen was proposed). The structural analysis now reported also allowed identification of putative formate and CO_2 tunnels, which will be probed in future studies using variants.

The reanalysis of the *E. coli* FdhH reduced structure[31] raised important questions regarding the mechanism of FDHs.[23] This reinterpretation of the original crystallographic data revealed that Sec is not coordinating the Mo in the formate-reduced structure and is found ∼9 Å away. Nevertheless, the poor electron density of the active site region suggests a possible mixture of states, where some Sec-Mo coordination may still be present.[23] This reinterpretation supports mechanisms that propose Sec/Cys displacement from the metal coordination during catalysis.[22,23,25,27,28] In contrast, the structure of the reduced DvFdhAB shows clearly that Sec remains bound to the metal in this redox state, suggesting a model of stable metal coordination during catalysis. Since all metal-dependent FDHs are likely to follow identical mechanisms, the Sec-displacement in reduced *E. coli* FdhH may be explained by corresponding to a transient state, or to the capture of an unproductive form of the enzyme due to labile metal coordination. Such labile coordination is supported by the observation that Sec/Cys can be alkylated with IAA in *E. coli* FdhH[39] and *R. capsulatus* Mo-FDH,[28] but not in DvFdhAB. Nevertheless, it should be pointed out that Sec/Cys alkylation by IAA may also occur even when metal coordination is maintained.[59] If the metal-Sec/Cys bond is indeed labile in some enzymes, then it remains to be determined whether this has mechanistic implications or is just incidental.

Other relevant changes are observed when comparing the DvFdhAB oxidized and reduced structures. In particular, there is a pronounced movement of conserved His193, together with a nearby helix and some aromatic residues close to the active site, which is likely to be mechanistically relevant. This is accompanied by a conformational change of the distal MGD2 (also observed in reduced EcFdhH), which agrees with the proposal that pyranopterins are noninnocent ligands, being probably involved in redox tuning of the metal.[54,60−62] Comparing the MGD cofactors in the structures of FDHs and nitrate reductases, there is a remarkable superposition of MGD1, involved in the electron transfer pathway (Figure S16). The contact of MGD1 with the FeS-0 center is mediated by a highly conserved lysine (Lys90 in DvFdhAB), which establishes a hydrogen bond with the exocyclic NH_2 of the pyranopterin. This conserved pathway is present both in FDHs and in the related nitrate reductases.[63] In contrast, the orientation and geometry of the distal MGD2 varies considerably among the homologous enzymes. These differences are accompanied by changes in the orientation of amino acid side chains that surround the extended cofactor. When comparing the DvFdhAB oxidized and reduced forms, the reorientation of the "bridging" Gln890 is noteworthy, suggesting a putative change in the redox state of the proximal pterin. Rothery et al. analyzed the conformations of 319 pyranopterins in 102 protein structures and concluded that the

https://dx.doi.org/10.1021/acscatal.0c00086
ACS Catal. 2020, 10, 3844−3856

electron-transfer MGD1 pyranopterin is in a tetrahydro oxidation state.[60] However, we consider that a mixture of pyranopterin redox states cannot be excluded. Interestingly, for arsenite oxidase the replacement of the structurally equivalent Gln residue to a Gly stabilized a Mo(V) state.[52] The same was reported for *E. coli* Nar,[53] where substitution of His1098 (corresponding to Gln890) by an Ala also increased the stability of the Mo(V) state. The structural changes observed in DvFdhAB together with mutagenesis data on other DMSOR family enzymes are congruent in showing the importance of the H-bond interactions bridging both pyranopterins in controlling the active site redox chemistry and catalysis. Although very high resolution (<1.5 Å) is required to assign the correct redox state to each pyranopterin, these observations raise the important point that computational predictions of enzymatic mechanisms should take into account also the putative redox role of the MGD cofactors.

CONCLUSIONS

In summary, we show that the recombinant DvFdhAB is a stable, highly active model system for CO_2 reduction. The structures reported here suggest that Sec remains bound to the metal during the catalytic cycle but clear changes in the second coordination sphere and in pyranopterin stabilization occur in the reduced enzyme. These changes include different H-bonding interactions between surrounding amino acids and both pyranopterins, agreeing with previous reports on the role of the pyranopterin in fine-tuning the metal redox potential and enzymatic activity. Our combined results do not support a mechanism of Sec/Cys dissociation from the metal, and agree with a second coordination sphere mechanism that may involve hydride transfer. Nevertheless, more detailed studies with future variants and new crystal structures will be required to allow further detailed insights into the catalytic mechanism, and production of improved engineered forms of this important enzyme.

MATERIALS AND METHODS

Expression of *fdhAB*. The vectors used for homologous expression and StrepII tag insertion of DvFdhAB were both constructed using the Sequence and Ligation Independent Cloning—SLIC—method, as described previously.[58] For the complementation vector plasmid pMO9075 was used as a source of the *Desulfovibrio* pBG1 replicon, the pUC origin of replication and the *aadA* gene, which confers resistance to spectinomycin − Sm^R. In this strategy the full *fdhA* gene, including the signal peptide sequence, and the C-terminal strepII tag, was introduced with the 21 bp ribosomal-binding site on the pMO9075 plasmid.[45] The primers were manufactured by Nzytech and are presented in Table S4. The fragments were treated separately with 0.5 U of T4 DNA polymerase (BioLabs Inc., New England), in the presence of 100 μg/mL of bovine serum albumin, for 60 min at room temperature, and the reaction was stopped by the addition of 1 mM dCTP. The treated fragments were mixed in a 1:1 molar ratio in T4 DNA ligase buffer (BioLabs Inc., New England) and incubated during 30 min at 37 °C. After a 10 min incubation on ice, 5 μL of the mixed fragments were transformed into 50 μL *E. coli* α-select Silver Efficiency (Bioline) and cells were plated on spectinomycin (100 μg/mL)-containing agar plates. The correct plasmid construct was screened by colony PCR and later confirmed by sequencing by GATC biotech, Germany.

For transformation, *D. vulgaris* and Δ*fdhAB* deletion strain were grown in MOY medium, with 30 mM sodium lactate/30 mM sodium sulfate (MOYLS) and 1.2 mM sodium thioglycolate. The constructed plasmids were then electroporated as previously described:[45] the suicide vector was electroporated with 1500 V, 250 Ω, and 25 μF on the wild-type strain to induce double recombination; the complementation vector was integrated in the Δ*fdhAB* deletion strain by electroporation with 1250 V, 250 Ω, and 25 μF (Gene Pulse Xcell, Bio-Rad). Transformed cells were left to recover overnight at 37 °C in 1 mL MOYLS medium and then plated inside the glovebox using MOYLS with 1.5% (w/v) agar, containing Geneticin G418 (400 μg/mL) and/or spectinomycin (100 μg/mL). Selected colonies were grown in liquid MOYLS and confirmed by PCR for *fdhB* gene. As a final confirmation, Strep-tagged DvFdhAB expression was verified by Western blot.

Organism and Growth Conditions. *D. vulgaris* Hildenborough (DSM 644) cells were grown in modified Postgate medium C containing 3.7 mM KH_2PO_4, 18.7 mM NH_4Cl, 17.6 mM Na_2SO_4, 0.4 mM $CaCl_2.2H_2O$, 0.24 mM $MgSO_4.7H_2O$, 1 g/L yeast extract, 26 μM $FeSO_4.7H_2O$, 1 mM sodium citrate tribasic dihydrate, 0.57 mM L-ascorbic acid, 0.88 mM sodium thioglycolate, 40 mM sodium formate, 10 mM sodium DL-lactate and 100 mM Tris base, supplemented with 1 μM of $NiCl_2 \cdot 6H_2O/Na_2SeO_3 \cdot 5H_2O$ and 0.1 μM of $Na_2O_4W \cdot 2H_2O$. In the case of the Δ*fdhAB* complemented-strain, the concentration of Ni, Se, and W was increased to 10 μM. Moreover, to limit the concentration of Mo in the medium, the amount of yeast extract used was reduced to 0.4 g/L. Growth was performed at 37 °C in a 300 L reactor with N_2 atmosphere. Cells were recovered by centrifugation and stored at −80 °C.

Western Blot. Cells were disrupted using BugBuster Protein Extraction Reagent (Novagen, Inc.). The soluble fraction was run on a 12% SDS-polyacrylamide gel and transferred to a polyvinylidene difluoride—PVDF—membrane for 1 h at 350 mA and 4 °C in a Mini Trans-Blot electrophoretic transfer cell (Bio-Rad). Membranes were blocked using PBS buffer with 3% BSA and 0.5% (v/v) Tween 20, and then washed in PBS buffer with 0.1% (v/v) Tween 20. The membrane was incubated with biotin blocking buffer (IBA Lifesciences, Germany) and then treated with Strep-Tactin antibody labeled with alkaline phosphatase (IBA Lifesciences, Germany) diluted 1:4000. After washing, immunodetection of bound antibodies was done, in the dark, by membrane treatment with ready-made solutions of nitro-blue tetrazolium and 5-bromo-4-chloro-3′-indolyphosphate—NBT-BCIP (Sigma), in 100 mM Tris-HCl pH 8.0, 100 mM NaCl, and 5 mM $MgCl_2$ buffer. Reaction was stopped by washing the membrane with distilled water.

Protein Purification. For $DvFdhAB^{WT}$ purification, cells were resuspended, in 20 mM Tris-HCl pH 7.6 and 10 mM $NaNO_3$ buffer, containing DNase, and disrupted in a French pressure cell in aerobic conditions. The crude extract was centrifuged at 8000*g* for 20 min at 4 °C, and the supernatant was further clarified by ultracentrifugation at 109 000*g* for 2 h at 4 °C. All the purification steps were performed at 4 °C aerobically. The soluble fraction was then loaded on a Q-sepharose high performance column, equilibrated with 20 mM Tris-HCl pH 7.6 with 10% (v/v) glycerol and 10 mM $NaNO_3$ (buffer A). Elution was carried out at a flow rate of 4 mL/min, with stepwise increments on NaCl concentration (50−20 mM steps, from 0 to 200 mM). The buffer of the fractions containing FDH activity (eluted around 150 mM NaCl) was exchanged to 20 mM KPi (K_2HPO_4/KH_2PO_4) buffer also with 10% (v/v) glycerol, and 10

https://dx.doi.org/10.1021/acscatal.0c00086
ACS Catal. 2020, 10, 3844−3856

mM $NaNO_3$ (buffer K), using a 30-kDa cutoff ultracentrifugation unit (Amicon Ultra-15 30K NMWL, Millipore). Then, 15% (v/v) $(NH_4)_2SO_4$ was added to the sample, which was further purified using a phenyl sepharose high performance column equilibrated with buffer K with 15% (v/v) $(NH_4)_2SO_4$. Elution was performed by reducing the ionic strength in a stepwise decreasing gradient with a flow rate of 2 mL/min. Pure DvFdhAB was eluted between 10.5 and 12% (v/v) $(NH_4)_2SO_4$, and the purity of the eluted fractions was evaluated by 12% SDS-polyacrylamide gel stained with Coomassie Brilliant Blue R-250.

For recombinant DvFdhAB affinity purification, cells were resuspended in 100 mM Tris-HCl pH 8.0 with 10% (v/v) glycerol, 10 mM $NaNO_3$, and 150 mM NaCl (buffer W). Cell disruption and soluble fraction clarification were performed as described above. The soluble fraction was then directly loaded on a Strep-tactin gravity flow (IBA Lifesciences, Germany) column equilibrated with buffer W. After five washing steps with buffer W, the recombinant protein was eluted with buffer W plus 2.5 mM D-desthiobiotin. The buffer of eluted samples was exchanged to buffer A and samples were stored, under nitrogen atmosphere, at 4 °C for immediate use, or −80 °C for longer periods. This column yields pure DvFdhAB as judged by 12% SDS-polyacrilamide gel.

Protein concentration was measured with the BCA Protein Assay Kit from Novagen, with bovine serum albumin as standard. The UV−visible absorption spectra of high purity oxidized sample was acquired on a UV-1800 Shimadzu spectrophotometer, and used to determine the molar extension coefficient. The UV−visible spectrum was also recorded for DvFdhAB after reduction with 20 mM formate, for 30 min, and with 1 mM dithionite, inside the glovebox. Routine UV−visible absorption spectra were obtained with a Nanodrop ND2000C. The molar extinction coefficient of the oxidized enzyme at 410 nm, was determined to be $\varepsilon_{410\ nm}$= 43 446 M^{-1} cm^{-1}.

Thermal Shift Assay. The melting temperature of DvFdhAB was determined using the Applied Biosystems Protein Thermal Shift Dye Kit: 1 to 2 mg/mL of pure enzyme, in buffer A or buffer T (20 mM Tris−HCl pH 7.6), was mixed with the dye (2−6× fold) and the melting curve recorded from 25 to 99 °C, on the QuantStudio 7 Flex Real-time PCR System from Applied Biosystems.

Activity Assays and Kinetic Analysis. Activity assays were performed with small adaptations from previously reported protocols.[42,43] FDH activity was determined using a UV-1800 Shimadzu spectrophotometer, inside a COY Anaerobic chamber, with an atmosphere of 2% H_2/98% N_2, at room temperature, with stirring. During assay optimization, different preincubations, their time, order of additions, and concentrations were tested. In the optimized method, the enzyme sample was preincubated with 50 mM DTT for 5 min prior to the reaction. Routinely, for formate oxidation measurements the reduction of 2 mM benzyl viologen was monitored at 555 nm ($\varepsilon_{578\ nm}$ (BV^+) = 12 mM^{-1} cm^{-1}), in 50 mM KPi pH 7.6 containing 1 mM DTT plus 20 mM sodium formate. One unit of oxidizing activity is defined as the amount of FDH capable of oxidizing 1 μmol of formate (reducing of 2 μmol of BV^{2+}) per min. For the reduction of CO_2, Zn-reduced methyl viologen was used as artificial electron donor. The oxidation of MV^+ (0.1 mM) was followed at 578 nm ($\varepsilon_{578\ nm}$ (MV^+) = 9.7 mM^{-1} cm^{-1}), in 50 mM KPi pH 6.9 with 1 mM DTT plus 50 mM sodium bicarbonate, as a source of CO_2 (after the addition of bicarbonate the pH rises to approximately 7.1). One unit of reducing activity is defined as the amount of FDH capable of reducing 1 μmol of CO_2 (oxidizing 2 μmol MV^+) per min. In assays with pure DvFdhAB a final concentration of 1.4 nM enzyme was used. The turnover numbers were calculated considering one catalytic active protomer $\alpha\beta$ (138 kDa). To evaluate inhibition by nitrate and azide, measurements were performed in the presence of 100 mM of nitrate or 10 mM of sodium azide.

The influence of pH on FDH activity was assessed using a buffer mix containing 100 mM glycine, K_2HPO_4, citric acid, and Tris. The pH was adjusted using HCl or KOH. The activity of the purified DvFdhAB was measured at substrate concentrations ranging from 0.5 μM to 10 mM sodium formate, at the optimum pH of 7.6. For the CO_2 reductase activity, concentrations of 75 μM to 50 mM sodium bicarbonate were employed at the optimum pH of 7.1 (see SI). In these assays, sodium bicarbonate was the last component to be added before starting the assay with the enzyme. Kinetic parameters were calculated by direct fitting of the Michaelis−Menten equation, using the least-squares method, using Graph Pad Prism 7.

Iodoacetamide Assays. The effect of iodoacetamide (IAA) was measured on the formate-oxidation activity. We could not measure the IAA effect on CO_2 reduction because IAA oxidizes MV^+ nonspecifically. As-isolated DvFdhAB was incubated for 30 min with 20 mM of IAA, alone or in the presence of 20 mM formate, or 20 mM nitrate, in 20 mM Tris HCl pH 7.6, 10% glycerol. After that, the IAA-treated samples were incubated for 5 min with DTT prior to measurement of formate oxidation activities.

For mass spectrometry analysis, 10 μg of IAA-treated DvFdhAB were digested with trypsin overnight at 37 °C. The resulting peptides were analyzed by LC−MS, with data acquired in positive TOF-MS mode using X500B QTOF (ABSciex) with Turbo V ion source (Sciex) mass spectrometer connected to the ExionLC AD UPLC system. External calibration was performed using β-galactosidase digest (ABSciex). The raw MS and MS/MS data were analyzed using the Explorer software of SCIEX OS-Q, the BioPharmaView software 3.0 (Sciex) and the Protein Pilot for peptide identification. Data were obtained by the Mass Spectrometry Unit (UniMS), ITQB/iBET, Oeiras, Portugal.

Crystallization, Data Collection, Structure Solution, and Refinement. For the crystallization of DvFdhAB, the commercial screens JBS 1, 2, 3, and 4 (Jena Biosciences) were used and 1 μL drops (1:1 protein:precipitant ratio) were dispensed using an Oryx8 crystallization robot (Douglas Instruments, Ltd.). The drops were set in 96 Well CrystalQuick X Plates (Greiner Bio-One) using the sitting-drop vapor diffusion method, and the plates were stored at 20 °C.

Thin needles appeared within 4 days on condition F11 (32% PEG 3350, 0.1 M Tris-HCl pH 8.5, 0.8 M LiCl) and were tested in situ using the home source (Bruker D8 Venture dual source X-ray generator equipped with a Photon 100 CMOS detector and the ISX stage). These crystals presented a protein diffraction pattern with very weak spots. In order to improve crystal quality and size, a scale up of the condition to 2 μL hanging drops was performed, with 1:1 protein/precipitant ratio, and the precipitant and salt concentrations were optimized. The best crystals appeared after 24 h with 32% PEG 3350, 0.1 M Tris-HCl pH 8.5, and 1 M LiCl. The crystals grew as thin plates to a maximum size of 0.1 × 0.2 × 0.05 mm^3 in 7 days.

The crystallization of DvFdhAB in the formate-reduced form was performed in an anaerobic chamber under an argon atmosphere at <0.1 ppm of oxygen, and all the solutions used were previously degassed and stored in the anaerobic chamber.

https://dx.doi.org/10.1021/acscatal.0c00086
ACS Catal. 2020, 10, 3844−3856

The protein was incubated with 10 mM of sodium formate, and the crystallization drops were prepared in the previously optimized condition (32% PEG 3350, 0.1 M Tris-HCl pH 8.5, 1 M LiCl). Crystals of the reduced form appeared after 1 week with the same shape of the oxidized form. The crystals were transferred into a cryoprotectant solution consisting of reservoir solution augmented with 20% (v/v) glycerol and then flash-cooled in liquid nitrogen.

X-ray diffraction data sets were collected at 100 K using a Pilatus 6M-F detectors on ID29[64] and ID30B[64] beamlines at the European Synchrotron Radiation Facility. The X-ray diffraction images were integrated with XDS,[65] and data were scaled and merged using CCP4 program Aimless.[66] The crystals of the oxidized form (DvFdhAB_ox) belong to space group $P2_12_12_1$ with unit cell parameters a = 64.59 Å, b = 127.64 Å, and c = 148.21 Å and diffracted beyond 2.1 Å. The structure was solved by molecular replacement with Phaser[67] using the structure of formate dehydrogenase from *Desulfovibrio gigas* to build the search model (PDB 1H0H). The two protein sequences share around 64% identity, and the search model was prepared with the CHAINSAW[68] tool from CCP4 software package, non-conserved residues were pruned down to the γ-atom. Crystals of the formate-reduced form (DvFdhAB_red) belong to the same space group with almost identical unit cell parameters a = 64.89 Å, b = 128.56 Å, and c = 149.63 Å and diffracted beyond 1.9 Å. The structure was also solved by molecular replacement but using the oxidized form as search model. Model building and refinement were performed with Coot[69] and phenix.refine.[70] The refined models for oxidized and reduced forms (PDB entries 6SDR and 6SDV) contain 1177 and 1181 amino acid residues, respectively, and were assessed using Molprobity (Table S2). Data processing and refinement statistics are presented in Table S2.

Tunnel Calculation. The program CAVER 3.0.1 was used as a PyMOL plugin[71] for calculating the tunnels in DvFdhAB, using manually adjusted settings. The initial starting point (S atom from W-SH), shell depth (2 Å), shell radius (3 Å), cluster threshold (3.5 Å), desired radius (5 Å), and maximum distance (3 Å) were maintained constant for all calculations. The maximum distance specifies the furthest point (from the initial point) to start a tunnel calculation. The bottleneck radius is the narrowest part of a given tunnel and corresponds to the minimum probe radius. The tunnel analysis provided a list of calculated tunnels that were ranked according to a specific cost function (e.g., for two tunnels with equal radii, the one with the shorter distances has a lower cost). The tunnel with the lowest cost was chosen as the primary tunnel.

Sequence Analyses. The amino acid sequence of *D. vulgaris* FdhA (UniProt- Q72EJ1) was used as query search against the UniProt reference proteomes via the Hidden Markov Model (HMM) profile implemented in the Phmmer web server.[72] The search was performed using default parameters and 6063 sequences were found (June 2019), which include a range of different Mo/W oxidoreductases. These sequences were subjected to multistep clustering based on sequence identity at 95% (5848 clusters), 75% identity (2599 clusters), and 50% identity (608 clusters)), using the h-CD-HIT software present in the CD-HIT web suite.[73]

A Maximum Likelihood (ML) phylogenetic tree was built based on a multiple sequence alignment of the 608 sequences representing each cluster, performed with the MAFFT software[74] using default options. Fourteen well-known FDH sequences were also included in the alignment (FdnG-1 and FdnG-2 from *D. vulgaris*; FdhA from *D. gigas*; Dde_0717 from *D. alaskensis*; Ddes_0555 from *D. desulfuricans*; Dret_0226 from *D. retbaense*; Sfum_0036 and Sfum_3510 from *S. fumaroxidans*; FdhA from *R. capsulatus*; FdnG from *C. necator*; FdhF from *T. kivui*; FdhF-2 from *A. woodii*; and FdnG and FdhF from *E. coli*). For inference and preparation of the phylogenetic tree, we used the MEGA X 10.1 software with default parameters.[75] FdhA proteins separate into two different branches in the phylogenetic tree.[55] One representing periplasmic NAD-independent FdhAs and containing 41 CD-HIT cluster representative sequences plus 10 known sequences (where *D. vulgaris* FdhA and *E. coli* FdhN and FdhO are included), and another representing cytoplasmic NAD-dependent FdhAs and containing 35 CD-HIT cluster representative sequences plus 4 known sequences (including *E. coli* FdhH). The multiple sequence alignment was edited using the Jalview software,[76] where gaps were trimmed using *D. vulgaris* FdhA as reference. The consensus logo (Figure S14) was created with Jalview, based on the alignment of the 51 sequences from the branch of NAD-independent FdhAs.

EPR Spectroscopy. EPR spectra were recorded at X-band on a Bruker Elexsys 500 spectrometer equipped with an Oxford Instruments ESR900 helium gas flow cryostat. Formate-reduced crystals of DvFdhAB, prepared as described above, were transferred to an EPR tube inside the glovebox (Jacomex). A solution sample of DvFdhAB (100 μL of 162 μM in Buffer A) was transferred to an EPR tube inside the glovebox and reduced by adding 20 μL of 60 mM sodium formate to the protein solution. EPR tubes were let to incubate for few minutes at room temperature, capped, transferred out of the glovebox, and frozen immediately in liquid nitrogen.

■ ASSOCIATED CONTENT

Supporting Information

This material is available free of charge on the ACS Publications Web site. The Supporting Information is available free of charge at https://pubs.acs.org/doi/10.1021/acscatal.0c00086.

> Plasmid sequence maps; Western blot of DvFdhAB-expressing strains; SDS-PAGE gel of purified DvFdhAB; UV−visible spectrum of of DvFdhAB; activity assays with different activation protocols; stability assays in different conditions; domains of DvFdhAB; electron density of DvFdhAB active site; EPR spectra of formate-reduced DvFdhAB in crystals and in solution; Gln890 environment in oxidized and reduced structures; formate and CO_2 tunnels; sequence conservation of residues lining the formate and hydrophobic tunnels; structural alignment of MGDs; calculations of dissolved CO_2 concentrations; crystallographic data processing and refinement statistics; reactivity of DvFdhAB cysteines with iodoacetamide; and primers (PDF)

■ AUTHOR INFORMATION

Corresponding Authors

Maria João Romão − *UCIBIO, Applied Molecular Biosciences Unit, Departamento de Química, Faculdade de Ciências e Tecnologia, Universidade Nova de Lisboa, 2829-516 Caparica, Portugal*; Email: mjr@fct.unl.pt

Inês A. Cardoso Pereira − *Instituto de Tecnologia Química e Biológica, Universidade Nova de Lisboa, 2780-157 Oeiras, Portugal*; orcid.org/0000-0003-3283-4520; Email: ipereira@itqb.unl.pt

https://dx.doi.org/10.1021/acscatal.0c00086
ACS Catal. 2020, 10, 3844−3856

Authors

Ana Rita Oliveira − *Instituto de Tecnologia Química e Biológica, Universidade Nova de Lisboa, 2780-157 Oeiras, Portugal*

Cristiano Mota − *UCIBIO, Applied Molecular Biosciences Unit, Departamento de Química, Faculdade de Ciências e Tecnologia, Universidade Nova de Lisboa, 2829-516 Caparica, Portugal*

Cláudia Mourato − *Instituto de Tecnologia Química e Biológica, Universidade Nova de Lisboa, 2780-157 Oeiras, Portugal*

Renato M. Domingos − *Instituto de Tecnologia Química e Biológica, Universidade Nova de Lisboa, 2780-157 Oeiras, Portugal*

Marino F. A. Santos − *UCIBIO, Applied Molecular Biosciences Unit, Departamento de Química, Faculdade de Ciências e Tecnologia, Universidade Nova de Lisboa, 2829-516 Caparica, Portugal*

Diana Gesto − *UCIBIO, Applied Molecular Biosciences Unit, Departamento de Química, Faculdade de Ciências e Tecnologia, Universidade Nova de Lisboa, 2829-516 Caparica, Portugal*

Bruno Guigliarelli − *Aix Marseille Université, CNRS, BIP, Laboratoire de Bioénergétique et Ingénierie des Protéines, Marseille 13402, France*

Teresa Santos-Silva − *UCIBIO, Applied Molecular Biosciences Unit, Departamento de Química, Faculdade de Ciências e Tecnologia, Universidade Nova de Lisboa, 2829-516 Caparica, Portugal*

Complete contact information is available at: https://pubs.acs.org/10.1021/acscatal.0c00086

Author Contributions

[‖]These authors contributed equally to this work.

Notes

The authors declare no competing financial interest.

■ ACKNOWLEDGMENTS

This work was financially supported by Fundação para a Ciência e Tecnologia (Portugal) through fellowship SFRH/BD/116515/2014 (to ARO), grant PTDC/BBB-EBB/2723/2014 (to I.A.C.P. and M.J.R.), and R&D units UID/Multi/04551/2013 (Green-IT), LISBOA-01-0145-FEDER-007660 (MostMicro) and (UID/Multi/04378/2019 (UCIBIO) cofunded by FCT/MCTES and FEDER funds through COMPETE2020/POCI. Funding from the European Union's Horizon 2020 research and innovation programme under grant agreement number 810856 is also acknowledged. The authors are also grateful to the EPR facilities available at the French EPR network (IR CNRS 3443) and the Aix-Marseille University EPR centre.

■ REFERENCES

(1) Appel, A. M.; Bercaw, J. E.; Bocarsly, A. B.; Dobbek, H.; DuBois, D. L.; Dupuis, M.; Ferry, J. G.; Fujita, E.; Hille, R.; Kenis, P. J. A.; Kerfeld, C. A.; Morris, R. H.; Peden, C. H. F.; Portis, A. R.; Ragsdale, S. W.; Rauchfuss, T. B.; Reek, J. N. H.; Seefeldt, L. C.; Thauer, R. K.; Waldrop, G. L. Frontiers, Opportunities, and Challenges in Biochemical and Chemical Catalysis of CO_2 Fixation. *Chem. Rev.* **2013**, *113* (8), 6621−6658.

(2) Takeda, H.; Cometto, C.; Ishitani, O.; Robert, M. Electrons, Photons, Protons and Earth-Abundant Metal Complexes for Molecular Catalysis of CO_2 Reduction. *ACS Catal.* **2017**, *7* (1), 70−88.

(3) Shi, J.; Jiang, Y.; Jiang, Z.; Wang, X.; Wang, X.; Zhang, S.; Han, P.; Yang, C. Enzymatic Conversion of Carbon Dioxide. *Chem. Soc. Rev.* **2015**, *44* (17), 5981−6000.

(4) Schuchmann, K.; Müller, V. Autotrophy at the Thermodynamic Limit of Life: A Model for Energy Conservation in Acetogenic Bacteria. *Nat. Rev. Microbiol.* **2014**, *12* (12), 809−821.

(5) Cotton, C. A.; Edlich-Muth, C.; Bar-Even, A. Reinforcing Carbon Fixation: CO_2 Reduction Replacing and Supporting Carboxylation. *Curr. Opin. Biotechnol.* **2018**, *49*, 49−56.

(6) Weiss, M. C.; Sousa, F. L.; Mrnjavac, N.; Neukirchen, S.; Roettger, M.; Nelson-Sathi, S.; Martin, W. F. The Physiology and Habitat of the Last Universal Common Ancestor. *Nat. Microbiol.* **2016**, *1* (9), 16116.

(7) Yishai, O.; Lindner, S. N.; Gonzalez de la Cruz, J.; Tenenboim, H.; Bar-Even, A. The Formate Bio-Economy. *Curr. Opin. Chem. Biol.* **2016**, *35*, 1−9.

(8) Singh, A. K.; Singh, S.; Kumar, A. Hydrogen Energy Future with Formic Acid: A Renewable Chemical Hydrogen Storage System. *Catal. Sci. Technol.* **2016**, *6* (1), 12−40.

(9) Romão, M. J. Molybdenum and Tungsten Enzymes: A Crystallographic and Mechanistic Overview. *Dalt. Trans.* **2009**, No. 21, 4053.

(10) Hartmann, T.; Schwanhold, N.; Leimkühler, S. Assembly and Catalysis of Molybdenum or Tungsten-Containing Formate Dehydrogenases from Bacteria. *Biochim. Biophys. Acta, Proteins Proteomics* **2015**, *1854* (9), 1090−1100.

(11) Maia, L. B.; Moura, I.; Moura, J. J. G. Molybdenum and Tungsten-Containing Formate Dehydrogenases: Aiming to Inspire a Catalyst for Carbon Dioxide Utilization. *Inorg. Chim. Acta* **2017**, *455*, 350−363.

(12) Niks, D.; Hille, R. Molybdenum- and Tungsten-Containing Formate Dehydrogenases and Formylmethanofuran Dehydrogenases: Structure, Mechanism, and Cofactor Insertion. *Protein Sci.* **2019**, *28* (1), 111−122.

(13) Reda, T.; Plugge, C. M.; Abram, N. J.; Hirst, J. Reversible Interconversion of Carbon Dioxide and Formate by an Electroactive Enzyme. *Proc. Natl. Acad. Sci. U. S. A.* **2008**, *105* (31), 10654−10658.

(14) Schuchmann, K.; Muller, V. Direct and Reversible Hydrogenation of CO_2 to Formate by a Bacterial Carbon Dioxide Reductase. *Science* **2013**, *342* (6164), 1382−1385.

(15) Maia, L. B.; Fonseca, L.; Moura, I.; Moura, J. J. G. Reduction of Carbon Dioxide by a Molybdenum-Containing Formate Dehydrogenase: A Kinetic and Mechanistic Study. *J. Am. Chem. Soc.* **2016**, *138* (28), 8834−8846.

(16) Schwarz, F. M.; Schuchmann, K.; Müller, V. Hydrogenation of CO_2 at Ambient Pressure Catalyzed by a Highly Active Thermostable Biocatalyst. *Biotechnol. Biofuels* **2018**, *11* (1), 237.

(17) Hartmann, T.; Leimkühler, S. The Oxygen-Tolerant and NAD^+-Dependent Formate Dehydrogenase from *Rhodobacter Capsulatus* Is Able to Catalyze the Reduction of CO_2 to Formate. *FEBS J.* **2013**, *280* (23), 6083−6096.

(18) Yu, X.; Niks, D.; Mulchandani, A.; Hille, R. Efficient Reduction of CO_2 by the Molybdenum-Containing Formate Dehydrogenase from *Cupriavidus Necator* (*Ralstonia Eutropha*). *J. Biol. Chem.* **2017**, *292* (41), 16872−16879.

(19) Thomé, R.; Gust, A.; Toci, R.; Mendel, R.; Bittner, F.; Magalon, A.; Walburger, A. A Sulfurtransferase Is Essential for Activity of Formate Dehydrogenases in *Escherichia Coli*. *J. Biol. Chem.* **2012**, *287* (7), 4671−4678.

(20) Arnoux, P.; Ruppelt, C.; Oudouhou, F.; Lavergne, J.; Siponen, M. I.; Toci, R.; Mendel, R. R.; Bittner, F.; Pignol, D.; Magalon, A.; Walburger, A. Sulphur Shuttling across a Chaperone during Molybdenum Cofactor Maturation. *Nat. Commun.* **2015**, *6* (1), 6148.

(21) Schrapers, P.; Hartmann, T.; Kositzki, R.; Dau, H.; Reschke, S.; Schulzke, C.; Leimkühler, S.; Haumann, M. Sulfido and Cysteine Ligation Changes at the Molybdenum Cofactor during Substrate Conversion by Formate Dehydrogenase (FDH) from *Rhodobacter Capsulatus*. *Inorg. Chem.* **2015**, *54* (7), 3260−3271.

(22) Robinson, W. E.; Bassegoda, A.; Reisner, E.; Hirst, J. Oxidation-State-Dependent Binding Properties of the Active Site in a Mo-Containing Formate Dehydrogenase. *J. Am. Chem. Soc.* **2017**, *139* (29), 9927−9936.

(23) Raaijmakers, H. C. A.; Romão, M. J. Formate-Reduced *E. Coli* Formate Dehydrogenase H: The Reinterpretation of the Crystal Structure Suggests a New Reaction Mechanism. *JBIC, J. Biol. Inorg. Chem.* **2006**, *11* (7), 849−854.

(24) Grimaldi, S.; Schoepp-Cothenet, B.; Ceccaldi, P.; Guigliarelli, B.; Magalon, A. The Prokaryotic Mo/W-BisPGD Enzymes Family: A Catalytic Workhorse in Bioenergetics. *Biochim. Biophys. Acta, Bioenerg.* **2013**, *1827* (8−9), 1048−1085.
(25) Mota, C. S.; Rivas, M. G.; Brondino, C. D.; Moura, I.; Moura, J. J. G.; Gonzalez, P. J.; Cerqueira, N. M. F. S. A. The Mechanism of Formate Oxidation by Metal-Dependent Formate Dehydrogenases. *JBIC, J. Biol. Inorg. Chem.* **2011**, *16* (8), 1255−1268.
(26) Tiberti, M.; Papaleo, E.; Russo, N.; De Gioia, L.; Zampella, G. Evidence for the Formation of a Mo−H Intermediate in the Catalytic Cycle of Formate Dehydrogenase. *Inorg. Chem.* **2012**, *51* (15), 8331−8339.
(27) Cerqueira, N. M. F. S. A.; Fernandes, P. A.; Gonzalez, P. J.; Moura, J. J. G.; Ramos, M. J. The Sulfur Shift: An Activation Mechanism for Periplasmic Nitrate Reductase and Formate Dehydrogenase. *Inorg. Chem.* **2013**, *52* (19), 10766−10772.
(28) Hartmann, T.; Schrapers, P.; Utesch, T.; Nimtz, M.; Rippers, Y.; Dau, H.; Mroginski, M. A.; Haumann, M.; Leimkuhler, S. The Molybdenum Active Site of Formate Dehydrogenase Is Capable of Catalyzing C-H Bond Cleavage and Oxygen Atom Transfer Reactions. *Biochemistry* **2016**, *55* (16), 2381−2389.
(29) Niks, D.; Duvvuru, J.; Escalona, M.; Hille, R. Spectroscopic and Kinetic Properties of the Molybdenum-Containing, NAD^+-Dependent Formate Dehydrogenase from *Ralstonia Eutropha*. *J. Biol. Chem.* **2016**, *291* (3), 1162−1174.
(30) Dong, G.; Ryde, U. Reaction Mechanism of Formate Dehydrogenase Studied by Computational Methods. *JBIC, J. Biol. Inorg. Chem.* **2018**, *23* (8), 1243−1254.
(31) Boyington, J. C.; Gladyshev, V. N.; Khangulov, S. V.; Stadtman, T. C.; Sun, P. D. Crystal Structure of Formate Dehydrogenase H: Catalysis Involving Mo, Molybdopterin, Selenocysteine, and an Fe_4S_4 Cluster. *Science* **1997**, *275* (5304), 1305−1308.
(32) Jormakka, M.; Tornroth, S.; Byrne, B.; Iwata, S. Molecular Basis of Proton Motive Force Generation: Structure of Formate Dehydrogenase-N. *Science* **2002**, *295* (5561), 1863−8.
(33) Raaijmakers, H.; Macieira, S.; Dias, J. M.; Teixeira, S.; Bursakov, S.; Huber, R.; Moura, J. J. G.; Moura, I.; Romao, M. J. Gene Sequence and the 1.8 Angstrom Crystal Structure of the Tungsten-Containing Formate Dehydrogenase from *Desulfovibrio gigas*. *Structure* **2002**, *10* (9), 1261−1272.
(34) George, G. N.; Colangelo, C. M.; Dong, J.; Scott, R.; Khangulov, S. V.; Gladyshev, V. N.; Stadtman, T. C. X-Ray Absorption Spectroscopy of the Molybdenum Site of *Escherichia coli* Formate Dehydrogenase. *J. Am. Chem. Soc.* **1998**, *120*, 1267−1273.
(35) George, G. N.; Costa, C.; Moura, J. J. G.; Moura, I. Observation of Ligand-Based Redox Chemistry at the Active Site of a Molybdenum Enzyme. *J. Am. Chem. Soc.* **1999**, *121*, 2625−2626.
(36) Khangulov, S. V.; Gladyshev, V. N.; Dismukes, G. C.; Stadtman, T. C. Selenium-Containing Formate Dehydrogenase H from *Escherichia Coli*: A Molybdopterin Enzyme That Catalyzes Formate Oxidation without Oxygen Transfer. *Biochemistry* **1998**, *37* (10), 3518−3528.
(37) Maia, L. B.; Moura, I.; Moura, J. J. G. *EPR Spectroscopy on Mononuclear Molybdenum-Containing Enzymes*; Springer: Cham, 2017; pp 55−101 DOI: 10.1007/978-3-319-59100-1_4.
(38) Grimaldi, S.; Biaso, F.; Burlat, B.; Guigliarelli, B. Electron Paramagnetic Resonance Studies of Molybdenum Enzymes. In *Molybdenum and Tungsten Enzymes: Spectroscopic and Theoretical Investigations*; Hille, R., Schulzke, C., Kirk, M. L., Eds.; Royal Society of Chemistry, 2016; pp 68−120.
(39) Axley, M. J.; Bock, A.; Stadtman, T. C. Catalytic Properties of an *Escherichia coli* Formate Dehydrogenase Mutant in Which Sulfur Replaces Selenium. *Proc. Natl. Acad. Sci. U. S. A.* **1991**, *88* (19), 8450−8454.
(40) Stams, A. J.; Plugge, C. M. Electron Transfer in Syntrophic Communities of Anaerobic Bacteria and Archaea. *Nat. Rev. Microbiol.* **2009**, *7* (8), 568−577.
(41) Plugge, C. M.; Zhang, W.; Scholten, J. C.; Stams, A. J. Metabolic Flexibility of Sulfate-Reducing Bacteria. *Front. Microbiol.* **2011**, *2*, 81.
(42) de Bok, F. A. M.; Hagedoorn, P. L.; Silva, P. J.; Hagen, W. R.; Schiltz, E.; Fritsche, K.; Stams, A. J. M. Two W-Containing Formate Dehydrogenases (CO_2-Reductases) Involved in Syntrophic Propionate Oxidation by *Syntrophobacter fumaroxidans*. *Eur. J. Biochem.* **2003**, *270* (11), 2476−2485.
(43) da Silva, S. M.; Voordouw, J.; Leitão, C.; Martins, M.; Voordouw, G.; Pereira, I. A. C. Function of Formate Dehydrogenases in *Desulfovibrio vulgaris* Hildenborough Energy Metabolism. *Microbiology (London, U. K.)* **2013**, *159* (8), 1760−1769.
(44) da Silva, S. M.; Pimentel, C.; Valente, F. M. A.; Rodrigues-Pousada, C.; Pereira, I. A. C. Tungsten and Molybdenum Regulation of Formate Dehydrogenase Expression in *Desulfovibrio vulgaris* Hildenborough. *J. Bacteriol.* **2011**, *193* (12), 2909−2916.
(45) Keller, K. L.; Wall, J. D.; Chhabra, S. Methods for Engineering Sulfate Reducing Bacteria of the Genus *Desulfovibrio*. *Methods Enzymol.* **2011**, *497*, 503−517.
(46) Niks, D.; Hille, R. Reductive Activation of CO_2 by Formate Dehydrogenases. *Methods Enzymol.* **2018**, *613*, 277−295.
(47) Almendra, M. J.; Brondino, C. D.; Gavel, O.; Pereira, A. S.; Tavares, P.; Bursakov, S.; Duarte, R.; Caldeira, J.; Moura, J. J. G.; Moura, I. Purification and Characterization of a Tungsten-Containing Formate Dehydrogenase from *Desulfovibrio gigas*. *Biochemistry* **1999**, *38* (49), 16366−16372.
(48) Bassegoda, A.; Madden, C.; Wakerley, D. W.; Reisner, E.; Hirst, J. Reversible Interconversion of CO_2 and Formate by a Molybdenum-Containing Formate Dehydrogenase. *J. Am. Chem. Soc.* **2014**, *136*, 15473−15476.
(49) Sokol, K. P.; Robinson, W. E.; Oliveira, A. R.; Warnan, J.; Nowaczyk, M. M.; Ruff, A.; Pereira, I. A. C.; Reisner, E. Photoreduction of CO_2 with a Formate Dehydrogenase Driven by Photosystem II Using a Semi-Artificial Z-Scheme Architecture. *J. Am. Chem. Soc.* **2018**, *140* (48), 16418−16422.
(50) Miller, M.; Robinson, W. E.; Oliveira, A. R.; Heidary, N.; Kornienko, N.; Warnan, J.; Pereira, I.; Reisner, E. Interfacing Formate Dehydrogenase with Metal Oxides for Reversible Electrocatalysis and Solar-Driven Reduction of Carbon Dioxide. *Angew. Chem.* **2019**, *131* (14), 4649−4653.
(51) Caillet-Saguy, C.; Turano, P.; Piccioli, M.; Lukat-Rodgers, G. S.; Czjzek, M.; Guigliarelli, B.; Izadi-Pruneyre, N.; Rodgers, K. R.; Delepierre, M.; Lecroisey, A. Deciphering the Structural Role of Histidine 83 for Heme Binding in Hemophore HasA. *J. Biol. Chem.* **2008**, *283*, 5960−5970.
(52) Duval, S.; Santini, J. M.; Lemaire, D.; Chaspoul, F.; Russell, M. J.; Grimaldi, S.; Nitschke, W.; Schoepp-Cothenet, B. The H-Bond Network Surrounding the Pyranopterins Modulates Redox Cooperativity in the Molybdenum-BisPGD Cofactor in Arsenite Oxidase. *Biochim. Biophys. Acta, Bioenerg.* **2016**, *1857* (9), 1353−1362.
(53) Wu, S. Y.; Rothery, R. A.; Weiner, J. H. Pyranopterin Coordination Controls Molybdenum Electrochemistry in *Escherichia coli* Nitrate Reductase. *J. Biol. Chem.* **2015**, *290* (41), 25164−25173.
(54) Rothery, R. A.; Weiner, J. H. Shifting the Metallocentric Molybdoenzyme Paradigm: The Importance of Pyranopterin Coordination. *JBIC, J. Biol. Inorg. Chem.* **2015**, *20*, 349−372.
(55) Magalon, A.; Ceccaldi, P.; Schoepp-Cothenet, B. The Prokaryotic Mo/W-BisPGD Enzymes Family. In *RSC Metallobiology—Molybdenum and Tungsten Enzymes: Biochemistry*; Hille, R., Schulzke, C., Kirk, M. L., Eds.; 2017; Vol. *2017*, pp 143−191 DOI: 10.1039/9781782623915-00143.
(56) Zorn, M.; Ihling, C. H.; Golbik, R.; Sawers, R. G.; Sinz, A. Selective SelC-Independent Selenocysteine Incorporation into Formate Dehydrogenases. *PLoS One* **2013**, *8* (4), No. e61913.
(57) Ma, S.; Caprioli, R. M.; Hill, K. E.; Burk, R. F. Loss of Selenium from Selenoproteins: Conversion of Selenocysteine to Dehydroalanine in Vitro. *J. Am. Soc. Mass Spectrom.* **2003**, *14* (6), 593−600.
(58) Marques, M. C.; Tapia, C.; Gutiérrez-Sanz, O.; Ramos, A. R.; Keller, K. L.; Wall, J. D.; De Lacey, A. L.; Matias, P. M.; Pereira, I. A. C. The Direct Role of Selenocysteine in [NiFeSe] Hydrogenase Maturation and Catalysis. *Nat. Chem. Biol.* **2017**, *13* (5), 544.

(59) Smee, J. J.; Goodman, D. C.; Reibenspies, J. H.; Darensbourg, M. Y. Models for Terminal Ni(S-Cysteine) Modification in [NiFe]-Hydrogenases by Iodoacetamide and Iodoacetate. *Eur. J. Inorg. Chem.* **1999**, *1999* (3), 539−546.
(60) Rothery, R. A.; Stein, B.; Solomonson, M.; Kirk, M. L.; Weiner, J. H. Pyranopterin Conformation Defines the Function of Molybdenum and Tungsten Enzymes. *Proc. Natl. Acad. Sci. U. S. A.* **2012**, *109* (37), 14773−14778.
(61) Gisewhite, D. R.; Yang, J.; Williams, B. R.; Esmail, A.; Stein, B.; Kirk, M. L.; Burgmayer, S. J. N. Implications of Pyran Cyclization and Pterin Conformation on Oxidized Forms of the Molybdenum Cofactor. *J. Am. Chem. Soc.* **2018**, *140*, 12808−12818.
(62) Jacques, J. G. J.; Fourmond, V.; Arnoux, P.; Sabaty, M.; Etienne, E.; Grosse, S.; Biaso, F.; Bertrand, P.; Pignol, D.; Léger, C.; Guigliarelli, B.; Burlat, B. Reductive Activation in Periplasmic Nitrate Reductase Involves Chemical Modifications of the Mo-Cofactor beyond the First Coordination Sphere of the Metal Ion. *Biochim. Biophys. Acta, Bioenerg.* **2014**, *1837*, 277−286.
(63) Moura, J. J. G.; Brondino, C. D.; Trincao, J.; Romao, M. J. Mo and W Bis-MGD Enzymes: Nitrate Reductases and Formate Dehydrogenases. *JBIC, J. Biol. Inorg. Chem.* **2004**, *9* (7), 791−799.
(64) McCarthy, A. A.; Barrett, R.; Beteva, A.; Caserotto, H.; Dobias, F.; Felisaz, F.; Giraud, T.; Guijarro, M.; Janocha, R.; Khadrouche, A.; et al. ID30B − a Versatile Beamline for Macromolecular Crystallography Experiments at the ESRF. *J. Synchrotron Radiat.* **2018**, *25* (4), 1249−1260.
(65) Kabsch, W. XDS. *Acta Crystallogr., Sect. D: Biol. Crystallogr.* **2010**, *66*, 125−132.
(66) Evans, P. R.; Murshudov, G. N. How Good Are My Data and What Is the Resolution? *Acta Crystallogr., Sect. D: Biol. Crystallogr.* **2013**, *69*, 1204−14.
(67) McCoy, A. J.; Grosse-Kunstleve, R. W.; Adams, P. D.; Winn, M. D.; Storoni, L. C.; Read, R. J. Phaser Crystallographic Software. *J. Appl. Crystallogr.* **2007**, *40*, 658−674.
(68) Stein, N. CHAINSAW: A Program for Mutating Pdb Files Used as Templates in Molecular Replacement. *J. Appl. Crystallogr.* **2008**, *41*, 641−643.
(69) Emsley, P.; Lohkamp, B.; Scott, W. G.; Cowtan, K. Features and Development of Coot. *Acta Crystallogr., Sect. D: Biol. Crystallogr.* **2010**, *66*, 486−501.
(70) Afonine, P. V.; Grosse-Kunstleve, R. W.; Echols, N.; Headd, J. J.; Moriarty, N. W.; Mustyakimov, M.; Terwilliger, T. C.; Urzhumtsev, A.; Zwart, P. H.; Adams, P. D. Towards Automated Crystallographic Structure Refinement with Phenix. Refine. *Acta Crystallogr., Sect. D: Biol. Crystallogr.* **2012**, *68*, 352−364.
(71) Chovancova, E.; Pavelka, A.; Benes, P.; Strnad, O.; Brezovsky, J.; Kozlikova, B.; Gora, A.; Sustr, V.; Klvana, M.; Medek, P.; Biedermannova, L.; Sochor, J.; Damborsky, J. CAVER 3.0: A Tool for the Analysis of Transport Pathways in Dynamic Protein Structures. *PLoS Comput. Biol.* **2012**, *8*, No. e1002708.
(72) Finn, R. D.; Clements, J.; Eddy, S. R. HMMER Web Server: Interactive Sequence Similarity Searching. *Nucleic Acids Res.* **2011**, *39*, W29−W37.
(73) Huang, Y.; Niu, B.; Gao, Y.; Fu, L.; Li, W. CD-HIT Suite: A Web Server for Clustering and Comparing Biological Sequences. *Bioinformatics* **2010**, *26* (5), 680−682.
(74) Katoh, K.; Misawa, K.; Kuma, K.; Miyata, T. MAFFT: A Novel Method for Rapid Multiple Sequence Alignment Based on Fast Fourier Transform. *Nucleic Acids Res.* **2002**, *30* (14), 3059−3066.
(75) Kumar, S.; Stecher, G.; Li, M.; Knyaz, C.; Tamura, K. MEGA X: Molecular Evolutionary Genetics Analysis across Computing Platforms. *Mol. Biol. Evol.* **2018**, *35* (6), 1547−1549.
(76) Waterhouse, A. M.; Procter, J. B.; Martin, D. M. A.; Clamp, M.; Barton, G. J. Jalview Version 2−a Multiple Sequence Alignment Editor and Analysis Workbench. *Bioinformatics* **2009**, *25* (9), 1189−1191.

https://dx.doi.org/10.1021/acscatal.0c00086
ACS Catal. 2020, 10, 3844−3856